A facile sol-gel synthesis and characterization of europium (Eu) doped β-$Bi_2Mo_2O_9$ nanoparticles with remarkably enhanced photocatalytic activity for waste-water treatments

Priyadharshini Shanmugam,[1] Thangaraju Dheivasigamani,[1*] S. Moorthy Babu,[2] S. AlFaify[3], Mohd. Shkir[3,4], R. Marnadu[5], Vasudeva Reddy Minnam Reddy*[6]

[1]nano-crystal Design and Application Lab (n-DAL), Department of Physics, PSG Institute of Technology and Applied Research, Coimbatore-641062, Tamil Nadu, India.
[2]Crystal Growth Centre, Anna University, Chennai, 600025, India
[3]Advanced Functional Materials & Optoelectronic Laboratory (AFMOL), Department of Physics, Faculty of Science, King Khalid University, P.O. Box 9004, Abha 61413, Saudi Arabia
[4]University Center for Research & Development (UCRD), Chandigarh University, NH95, Chandigarh-Ludhiana Highway, Gharuan, Mohali, Punjab 140413 India
[5]PG Department of Physics, G.T.N. Arts College, Dindigul 624 005, Tamil Nadu, India
[6]School of Chemical Engineering, Yeungnam University, Gyeongsan 38541, Republic of Korea

DRAFT

*Corresponding author Dheivasigamani Thangaraju

E-mail: thangaraju@psgitech.ac.in

*Co corresponding author Vasudeva Reddy Minnam Reddy

e-mail: drmvasudr9@gmail.com

*Submitting author

shkirphysics@gmail.com

ABSTRACT

A facile sol-gel technique was employed to synthesise the nanoparticles of β-$Bi_2Mo_2O_9$ in acidic and water medium and Eu doped β-$Bi_2Mo_2O_9$ in acidic medium. The crystalline structure of the synthesised nanoparticles was characterized by powder X-ray Diffractometry, thereby confirming the presence of monoclinic structure of pure β-$Bi_2Mo_2O_9$ and Eu doped β-$Bi_2Mo_2O_9$. Raman analysis was performed to verify the phase purity and to identify the vibrational modes of synthesised pure and doped molybdates. The surface morphology of synthesised particles was examined using scanning electron microscopy, which shows the formation of a honeycomb-like structure with numerous pores in it. UV-visible spectroscopy and XPS were involved to the study of optical properties of synthesised nanoparticles. The dye degradation process demonstrated the photocatalytic activity under visible light radiation in which Methylene blue acts as a model dye. The change in the absorbance of the dye with synthesised β-$Bi_2Mo_2O_9$ and Eu doped β-$Bi_2Mo_2O_9$ with different concentrations of Eu^{3+} were studied by UV-Visible spectrophotometer. The results indicate that the water-based β-$Bi_2Mo_2O_9$ shows more dye degradation than acidic-based β-$Bi_2Mo_2O_9$.The increase in photocatalytic activity of acidic-based β-$Bi_2Mo_2O_9$ was achieved by the doping of Eu^{3+} and the efficiency increases with increase in doping percentage of Eu^{3+}. The 10% Eu:$Bi_2Mo_2O_9$ completely degraded the Methylene Blue dye (100%) within a period of 4hours.

Keywords: Photocatalytic, Molybdates, Methylene Blue, Dye degradation

DRAFT

1. Introduction

Nearly ten thousand dyes and their combinations were applied to add permanent colour to textile fibres which resist sweat, light, oxidising agents and microbial attack. To fulfil the modern fashion industry's requirements, textile manufacturers produce a wide variety of coloured garments by introducing numerous toxic dye chemicals. Used indestructible, complex structured, and greatly dispersible dyes are mixed with the water systems and affect terrestrial and aquatic ecosystems [1]. These carcinogenic organic dyes put forth severe environmental problems that risk the lives of humankind [2–4]. The biological treatment of dyes is limited due to pollutant's high chemical oxygen demand (COD) and is highly harmful to microbial cells [5]. Traditional wastewater treatment methods, including reverse osmosis and chemical oxidation, also failed to exclude these organic dyes [6,7]. This makes the researchers seek environmentally friendly and efficient methods to eliminate these toxic effluents.

Semiconductor photocatalyst paves the way for the decomposition of organic compounds by the photocatalytic method as it has tunable bandgap and potent catalytic properties [8–10]. The transition metal oxides have high resistivity, while post-transition metal oxides have low visible light absorption due to their indirect bandgap. Bi-based semiconductor photocatalysts, including bismuth oxide [11], bismuth molybdate [12,13], bismuth tungstate [14], bismuth vanadate [15,16], are immensely attractive as they have a low bandgap which can assist in visible light energy. The catalyzing, ion exchange, and light-emitting properties have drawn more interest towards the Aurivillus phase catalyst Bismuth molybdate [17–19]. The Bismuth molybdates occur in three phases, namely α –$Bi_2Mo_3O_{12}$, β- $Bi_2Mo_2O_9$, and ϒ -Bi_2MoO_6 [20–22]. The α-$Bi_2Mo_3O_{12}$ and β- $Bi_2Mo_2O_9$ phases are usually used for selective oxidation of hydrocarbons, while ϒ-Bi_2MoO_6 has been used in the photocatalytic breakdown of wastewater with the evolution of O_2 under a visible light source. The defective scheelite structure is exhibited by α-$Bi_2Mo_3O_{12}$ in which one of three Bi sites is unoccupied [23], whereas the β-

DRAFT

$Bi_2Mo_2O_9$ appears to be defective fluorite form with unfilled metal sites [24]. The ϒ-Bi_2MoO_6 exhibits the arrangement of $(Bi_2O_2)^{2+}$ sheets with perovskite layers of $(MoO_4)^{2-}$ [25]. Although at a temperature of about 500-675ºC, the β phase remains stable, at a temperature of about 500-670ºC, it forms α and ϒ phases [26]. Though these three phases of bismuth molybdate act as an excellent photocatalyst under visible light, the high recombination rate of photogenerated charge carriers [27–29] and the poor light absorption efficiency [30] limit its photocatalytic activity. This can be overcome by the doping of ions which can effectively restrain the recombination of photo-generated electron-hole pairs, leading to a high photocatalytic efficiency [31]. Following this, the photocatalytic performance of Bi_2MoO_6 was improved by Te doping [32]. Similarly, the doping of W^{6+} on Bi_2MoO_6 and Fe^{3+} on $Bi_2Mo_2O_9$ exhibit better photocatalytic activity [33,34]. The formation of highly uniform nanoparticles can be achieved at low temperatures by using the sol-gel method, which is one of the most facile and inexpensive synthesis techniques [35,36].

In this work, the sol-gel technique was employed to synthesise the nanoparticles of β-$Bi_2Mo_2O_9$ in acidic and water medium and Eu doped β-$Bi_2Mo_2O_9$ in acidic medium. The structural, compositional and the morphological analysis of the synthesised nanoparticles were conducted by XRD, RAMAN and SEM. The optical properties of β-$Bi_2Mo_2O_9$ and Eu doped β-$Bi_2Mo_2O_9$ was studied using UV-visible spectroscopy and XPS. The photocatalytic activity of β-$Bi_2Mo_2O_9$ in acidic and water media, as well as Eu doped $Bi_2Mo_2O_9$ at various concentrations of Eu^{3+}, was investigated in detail.

2. Experimental Methods

2.1 Materials

DRAFT

Bismuth (III) nitrate pentahydrate ($Bi(NO_3)_3.5H_2O$, Merck), Ammonium heptamolybdate tetrahydrate ($(NH_4)_6Mo_7O_{24}.4H_2O$, Merck), Europium nitrate hexahydrate ($Eu(NO_3)_3.6H_2O$), Citric acid monohydrate ($C_6H_8O_7.H_2O$, Sisco), Acetic acid (CH_3COOH, Nice Chemicals), and Ethylene glycol ($C_2H_6O_2$, Hi Media) were used without any further purification. The photocatalytic activity was studied using methylene blue as a model pollutant.

2.2 Photocatalyst preparation

Synthesis of bismuth molybdate nanoparticles in two different media and Eu doped bismuth molybdate nanoparticles was carried out by the sol-gel method. In particular, 1.75 mmole of Bismuth (III) nitrate pentahydrate ($Bi(NO_3)_3.5H_2O$) and 0.25 mmole of Ammonium heptamolybdate tetrahydrate ($(NH_4)_6Mo_7O_{24}.4H_2O$) were dissolved in 5mL and 45mL of deionized water, respectively and stirred for a while in a separate beaker. These two solutions were then combined forming a clear solution. The solution mixture was then treated with 2 mmole of citric acid monohydrate ($C_6H_8O_7.H_2O$). It forms the citrate complex as citric acid combines with metal ions in a mixed solution [37]. The citrate complexes were combined by adding four drops of ethylene glycol ($C_2H_6O_2$), which acts as an inducing agent to polymerize the complexes [38,39]. The resultant solution was stirred for 8 hours at a temperature of about 70 °C. The collected suspension liquid gel was subjected to preheating at 250 °C in a muffle furnace. Then, the conducted samples were annealed at 550°C for an hour. The reactor was allowed to cool at room temperature and the obtained powder was yellow in colour. The same procedure was adopted to synthesise $Bi_2Mo_2O_9$ in acetic acid medium and Europium doped $Bi_2Mo_2O_9$ with different percentages of Europium nitrate hexahydrate. In particular, 1.66 mmole of Bismuth (III) nitrate pentahydrate ($Bi(NO_3)_3.5H_2O$) was dissolved in 5 mL of acetic acid and the 5% of Europium nitrate hexahydrate ($Eu(NO_3)_3.6H_2O$) was added to it. It was then mixed with 0.25 mmole of $(NH_4)_6Mo_7O_{24}.4H_2O$ which was dissolved in 45 mL of deionized water. Then the previous procedures were adopted and as a result, the yellow-coloured Eu

DRAFT

doped $Bi_2Mo_2O_9$ nanoparticles were obtained. The synthesis was repeated for 10% Eu doped $Bi_2Mo_2O_9$.

2.3 Characterisation techniques

The phase and crystallinity of synthesised β- $Bi_2Mo_2O_9$ nanoparticles and Eu doped $Bi_2Mo_2O_9$ nanoparticles were studied by 'X'PERT PANalytical Powder X-ray Diffraction (PXRD) with CuKα radiation of λ=1.5405Å. Raman spectral study was done by Jobin Yuvon HR 800 Raman spectrometer with a laser source of about 532nm. The band gap of the photocatalyst was studied using diffuse reflectance with a Thermofisher UV–visible spectrophotometer. The morphology of the surface of synthesised nanoparticles was examined by a ZESS EVO 18 scanning electron microscope. X-ray photoelectron spectroscopy (XPS) was performed by Thermo Scientific K-Alpha Surface Analysis with an Al source to identify the constituents of synthesised nanoparticles. The photocatalytic behaviour β- $Bi_2Mo_2O_9$ and Eu doped $Bi_2Mo_2O_9$ nanoparticles was investigated by identifying the change in absorbance intensity of methylene blue dye using a Shimadzu – 1380 UV/Vis-NIR spectrophotometer.

2.4 Dye degradation experiment

The reduction of methylene blue using a UV-visible light source was used to measure the photocatalytic activity of the β- $Bi_2Mo_2O_9$ in acidic and water medium and the Eu doped $Bi_2Mo_2O_9$. 50 mg of the catalyst was added to 50ml of methylene blue solution (10 mg/L) and it was stirred continuously using the magnetic stirrer. A glass reactor with an inlet and outlet jacket for water circulation was used for the dye degradation experiment. The height between the reactor bottom and the light source was maintained constant throughout the experiments. To attain absorption equilibrium, the dark stirring of the solution was performed for about 1hour. Then the solution is subjected to illumination of light for about 4 hours and 5 ml of sample solution is collected at a regular interval of 1 hour. Then, the collected samples were

DRAFT

centrifuged at a speed of 3500rpm for 3 minutes to remove the suspended particles. A UV-Visible spectrophotometer was used to evaluate the change in the absorbance curve of the dye, which has a maximum absorption peak of 664nm. The degradation percentage of methylene blue was calculated by

$$\text{Degradation percentage} = \frac{A_0 - A_t}{A_0} \times 100\% \quad (1)$$

where A_0 is initial absorbance and A_t is the absorbance at a particular time.

2.5 Photocatalytic kinetic model

The kinetics study of the methylene blue degradation process is studied by using three different models namely first order model, diffusion model and Singh model [40].

The first order model is given by

$$-\frac{dC}{dt} = k_1 C \quad (2)$$

When the known limits are substituted and integrated, the given model become

$$ln\left(\frac{C_0}{C}\right) = k_1 t \quad (3)$$

where k_1 is the pseudo-first-order rate constant, C_0 and C are the initial and final concentrations of methylene blue, respectively and t be the time of the light illuminated.

The diffusion model is given by

$$-\frac{dC}{dt} = k_2 C^{0.5} \quad (4)$$

The above equation becomes as follows, when it is integrated between the specified limits.

$$\sqrt{C} - \sqrt{C_0} = \frac{k_2}{2} t \quad (5)$$

DRAFT

where k_2 is the rate constant for diffusion model, C_0 and C are the initial and final concentrations of methylene blue, respectively and t be the time of the light illuminated.

The Singh model is given by

$$-\frac{dC}{dt} = \frac{k_3 C}{1+t} \tag{6}$$

By substituting and integrating the known limits, the model becomes,

$$ln\left(\frac{C}{C_0}\right) = k_3 ln(1+t) \tag{7}$$

where k_3 is the rate constant for Singh model, C_0 and C are the initial and final concentrations of methylene blue, respectively and t be the time of the light illuminated.

3. RESULT AND DISCUSSION

3.1 Structural studies

Acquired XRD pattern of pure β- $Bi_2Mo_2O_9$ nanoparticles in an acidic medium which annealed @250°C and 500°C, 5%Eu: $Bi_2Mo_2O_9$ @500°C (acidic medium), 10%Eu: $Bi_2Mo_2O_9$ @500°C (acidic medium), $Bi_2Mo_2O_9$ @500°C (water medium) were shown in Figure 1. The observed patterns were well fitted with the standard monoclinic structure of $Bi_2Mo_2O_9$ (JCPDS card no.01-084-0829) with a space group of P21/n. The lattice constants were a = 11.9720, b =10.8130, and c =11.8990. The $Bi_2Mo_2O_9$ annealed at 250 °C in an acidic medium exhibits a low intense reflection peak. After 500 °C annealing, a sharp peak in the (023) plane is observed. The $Bi_2Mo_2O_9$ @500°C shows the intense peak at diffracting angles of 28.2, 31.8, 32.5, 36.2 and 46.5 in (023), (303), (040), (240) and (-343) planes, respectively. Thus, the annealing temperature effectively modifies the growth of the plane in $Bi_2Mo_2O_9$. The doping of Eu^{3+} into $Bi_2Mo_2O_9$ eliminates a small amount of Bi_2MoO_6, indicating that Eu^{3+} promotes the effective growth of $Bi_2Mo_2O_9$.

DRAFT

3.2 Raman spectral analysis

Figure 2 shows the Raman spectrum of $Bi_2Mo_2O_9$@500 °C (Acidic medium), 5%Eu: $Bi_2Mo_2O_9$ @500°C (acidic medium), 10%Eu: $Bi_2Mo_2O_9$ @500°C (acidic medium) and $Bi_2Mo_2O_9$ @500°C (water medium). The $2A_{1g} + B_{1g} + 3E_g$ are the six Raman active modes, and $4A_{2u} + 5E_u$ are the nine IR active modes of the ideal structure [41]. The characteristic peaks at 120, 289, 305, 891, 1794, 1940 and 2503 cm^{-1} are observed in spectra. The translation motions of Bismuth and Molybdenum atoms give the peak at 81cm^{-1}. The peak at 286cm^{-1} reveals the bending mode of MoO_6 of different components [42]. The peak at 821cm^{-1} and 925 cm^{-1} occurs due to the stretching mode of Mo-O. The lattice mode of Bi^{3+} atoms in the perpendicular direction to the layers specifies the peak at 891cm^{-1}. The lower intensity peaks at 120 cm^{-1}, 289 cm^{-1}, 305 cm^{-1} occur due to the bending motion of O-M-O. The structural disorder induces the strong interaction between Eu^{3+} and the host $Bi_2Mo_2O_9$ and is also responsible for the changes in bond angle and length.

3.3 Energy gap evaluation

The band gap of $Bi_2Mo_2O_9$ and 5, 10% Eu doped $Bi_2Mo_2O_9$ was determined using Tau's relation for direct band gap material and it is given as follows.

$$(\alpha h\upsilon)^2 = A(h\upsilon - E_g) \tag{8}$$

where α is the absorption coefficient, $h\upsilon$ is photon energy and E_g is the band gap of the material [43,44]. Figure 3 shows the plot between $(\alpha h\upsilon)^2$ and $h\upsilon$ which helps to calculate the band gap of the synthesised nanoparticles. The E_g values of $Bi_2Mo_2O_9$ and 5, 10% Eu doped $Bi_2Mo_2O_9$ synthesised in acetic medium were estimated to be 3.02, 2.98 and 2.95 eV respectively. The doping of Eu^{3+} to $Bi_2Mo_2O_9$ narrows its band gap and the band gap energy decreases as the doping percentage of Eu^{3+} increases.

DRAFT

3.4 XPS analysis

The elemental composition and the oxidation state of the synthesized $Bi_2Mo_2O_9$ and 10% Eu doped $Bi_2Mo_2O_9$ was examined using XPS. Figure 4(a) and 4(b) depicts the spectra of Bi and Mo in pure and doped $Bi_2Mo_2O_9$. The characteristic peaks obtained in the individual XPS spectra of Bi4f, Mo3d, Eu3d and O1s ascertain the formation of bismuth molybdate. The as synthesized $Bi_2Mo_2O_9$ exhibits two definite peaks with binding energies of around 165.1ev for Bi $4f_{4/2}$ and 159.83eV for $Bi4f_{7/2}$. The shift in the characteristic peak is observed, when Eu is doped with $Bi_2Mo_2O_9$. The definite peaks of Eu doped $Bi_2Mo_2O_9$ has binding energy of about 165.6 eV for Bi $4f_{4/2}$ and 160.30 eV for $Bi4f_{7/2}$. Figure 4(b) shows the peaks with the binding energy of 235.8 eV and 232.7 eV which corresponds to $Mo3d_{3/2}$ and $Mo3d_{5/2}$ respectively [45]. The two intense peaks in MO 3d spectrum of Eu incorporated $Bi_2Mo_2O_9$ attributes to $Mo3d_{3/2}$ and $Mo3d_{5/2}$ of corresponding 236.4 eV and 233.3 eV with a minimal shift. The O1s spectrum of undoped and doped $Bi_2Mo_2O_9$ (Figure 4(c)) has one significant peak due to bonding of Bi-O and Mi-O. The O1s peak with binding energy of 531.eV for Eu doped $Bi_2Mo_2O_9$ seems to be shifted in comparison with $Bi_2Mo_2O_9$. Figure 4(d) shows Eu 3d spectrum of 10% Eu doped $Bi_2Mo_2O_9$ with one characteristic peak around 1135.3 eV of Eu $3d_{5/2}$ [46]. The result implies that Eu are in the Eu3+ oxidation state.

3.5 Surface Morphology

Figures 5(a-d) and 6(a & b) show SEM images of $Bi_2Mo_2O_9$ @500°C in an acidic medium, respectively, while Figures 6(c & d) show $Bi_2Mo_2O_9$ @500°C in a water medium. The samples exhibited an ordered honeycomb-like structure in which several microporous openings grew perpendicularly to the surface. Every pore unit is made up of several inner-grown porous structures. Furthermore, the formation of the interconnected open-framework structures grown at high annealing temperatures is observed. It is deduced that the microporous are inside the

DRAFT

walls of the macroporous, originating from the honeycomb holes. The water-based $Bi_2Mo_2O_9$ exhibits a spiral-like arrangement of porous inside the honeycomb-like structure. Compared to the water medium, the acetic-based $Bi_2Mo_2O_9$ has a small porous and the number of porous is also less. Figure 5(e-h) shows the surface morphology of the synthesized 5%Eu: $Bi_2Mo_2O_9$@500 ℃, while the Figure 5(i-l) shows the morphology of 10%Eu: $Bi_2Mo_2O_9$@500ºC. The Eu doped $Bi_2Mo_2O_9$ nanoparticles also exhibit an ordered honeycomb-like structure with microporous. The numerous small dots with a uniform dispersion were identified to be Eu^{3+} nanoparticles that reside inside the walls of honeycomb holes. Thus, the addition of Eu^{3+} causes excess defects on its surface, thereby increasing the number of porous. The porous structures contribute to greater surface area, lower density, making them useful for light harvesting, electron/ion transport, and mass diffusion, thereby providing a favourable condition for photocatalytic applications [47].

3.6 Evaluation of Photocatalytic activity of $Bi_2Mo_2O_9$

The photocatalytic activity of $Bi_2Mo_2O_9$ in acidic and water medium and Eu doped $Bi_2Mo_2O_9$ at various concentrations was investigated using a dye degradation process with methylene blue as a model dye. The UV-Visible spectra, which shows the change of absorption intensity of methylene blue solution photocatalysed by β-$Bi_2Mo_2O_9$ and Eu doped β-$Bi_2Mo_2O_9$ with different irradiation time is depicted in Figure 6.The characteristic absorption peak intensity of methylene blue at 664nm is gradually decreased, revealing that methylene blue was oxidised and reduced when a photon collided with a semiconducting catalyst. The degradation percentage of methylene blue by β-$Bi_2Mo_2O_9$ synthesised in water and acidic medium and the Eu doped at different concentrations was calculated using equation (1) [48] and it was plotted against time, which is shown in Figure 7. The methylene blue degradation by β-$Bi_2Mo_2O_9$ in acidic and water medium was 90% and 97%, respectively The photocatalytic activities of 5 and 10% Eu-doped $Bi_2Mo_2O_9$ in acidic medium were up to 95% and 99%, respectively. This

DRAFT

reveals that the doping of Eu to β-$Bi_2Mo_2O_9$ enhanced the photocatalytic activity of β-$Bi_2Mo_2O_9$ in acidic medium, thereby increasing its dye degradation efficiency than β-$Bi_2Mo_2O_9$.Compared with the acidic-based $Bi_2Mo_2O_9$, the water-based $Bi_2Mo_2O_9$ shows higher photocatalytic degradation efficiency. Though the water-based $Bi_2Mo_2O_9$ degrades the dye effectively, it does not degrade the dye entirely at the end of 4 hours. The doping of rare earth ions was done to increase the efficiency of acidic-based $Bi_2Mo_2O_9$. It can be seen that the addition of Eu to acidic-based $Bi_2Mo_2O_9$ increases the degradation efficiency. The addition of dopants to nanoparticles will decrease the recombination of electron-hole pairs and increase the active area sites of nanoparticles, which significantly helps in photocatalytic performance, resulting in enhanced dye degradation. Further, the degradation efficiency changes to a higher value as the Eu concentration increases, such that 10%Eu: $Bi_2Mo_2O_9$ attained complete degradation in 4 hours. The comparison of photocatalytic activity of $Bi_2Mo_2O_9$ with other phases of bismuth molybdate was tabulated in table 1.

The better photocatalytic results were obtained by the synthesised $Bi_2Mo_2O_9$ and Eu doped $Bi_2Mo_2O_9$. The photoexcitation process occurs when the $Bi_2Mo_2O_9$ photocatalyst is exposed to light with an energy greater than or equal to the energy of its band gap. This generates the electron hole pairs (e^- and h^+) by moving electrons from the valence band to the conduction band. The induced photoelectrons have greater reducing power and so when they are captured by electron acceptors such as O_2, it results in the formation of superoxide radical anion (O_2^-). The photoinduced electrons are said to have a stronger reducing capacity if they have their CB in more negative energy level while the photoinduced holes have greater oxidation power when their VB is at more positive energy level. The induced holes are easily captured by the electronic donors, resulting in an oxidation process. Thus, the reactive species $\cdot O_2^-$ and $\cdot OH$ helps in the degradation of MB molecules [49]. The doping of rare earth metals (Eu^{3+}) into $Bi_2Mo_2O_9$ results in the formation of a localised energy level in the band structure, which may

DRAFT

be used to explain the favourable impact of the Eu^{3+} dopant [50]. The changes in the band structure will affect the charge transition between the HOMO (valence band) and LUMO (conduction band) of $Bi_2Mo_2O_9$ and also the 4f and 5d electrons of Eu^{3+} influence the bandgap. Also, the dopant in the matrix may function as an electron-hole trap that will affect the recombination rate of induced electrons and holes. The reaction mechanism is as follows:

$$Bi_2Mo_2O_9 + hv \rightarrow Bi_2Mo_2O_9\ (e^- + h^+) \quad (8)$$

$$H_2O + Bi_2Mo_2O_9\ (h^+) \rightarrow Bi_2Mo_2O_9 + {}^{\cdot}OH + H^+ \quad (9)$$

$$Eu^{3+} + O_2 \rightarrow Eu^{4+} + {}^{\cdot}O_2{}^- \quad (10)$$

$$Bi_2Mo_2O_9\ (e^-) + Eu^{4+} \rightarrow Bi_2Mo_2O_9 + Eu^{3+} \quad (11)$$

$${}^{\cdot}O_2{}^- + H^+ \rightarrow {}^{\cdot}HO_2 \quad (12)$$

$${}^{\cdot}HO_2 + {}^{\cdot}HO_2 \rightarrow H_2O_2 + O_2 \quad (13)$$

$$H_2O_2 + {}^{\cdot}O_2{}^- \rightarrow {}^{\cdot}OH + OH^- + O_2 \quad (14)$$

$$MB + {}^{\cdot}OH/{}^{\cdot}O_2{}^-/H_2O_2 \rightarrow \text{degraded products} \quad (15)$$

Figure 8 depicts the kinetics study of the methylene blue degradation process using three different models, namely first order, diffusion and the Singh model. Table 2 shows the rate constant and the R^2 value for the synthesised photocatalysts for the above mentioned models. From the first order model, the rate constant value for $Bi_2Mo_2O_9$ in water medium was found to be 1.488 $hour^{-1}$, which is greater than that of other synthesised photocatalysts. The diffusion and Singh models also reveal that the $Bi_2Mo_2O_9$ in the water medium degrades methylene blue at a faster rate with k values of -0.311 and -2.987, respectively. The coefficient of determination R^2 gives the measure of how well a model fits the data. The R^2 value for $Bi_2Mo_2O_9$ in the water medium for first order was found to be 0.9876. This indicates that the first order model was well fitted with the data and the negative rate constant of diffusion and the Singh model shows that they were unable to explain the degradation process. Thus the degradation of methylene blue by the synthesised phototcatalysts follows the first order kinetic model.

DRAFT

4. CONCLUSION

The β-$Bi_2Mo_2O_9$ in acidic and water medium and Eu doped β- $Bi_2Mo_2O_9$ with different concentrations of Eu^{3+} were successfully synthesised by the sol-gel method. The monoclinic structure of the synthesised nanoparticles was confirmed by the powder XRD technique. Raman spectroscopy was used to confirm phase purity and detected the vibrational modes of β- $Bi_2Mo_2O_9$ and Eu doped $Bi_2Mo_2O_9$. SEM images revealed a honeycomb-like structure of β-$Bi_2Mo_2O_9$ and Eu doped $Bi_2Mo_2O_9$ with numerous microporous in it. The band gap of the synthesised nanoparticles was calculated and their optical properties were studied using UV-visible spectroscopy and XPS. The degradation of methylene blue, which was performed to assess the photocatalytic activity of the catalyst, shows that the water-based $Bi_2Mo_2O_9$ shows more efficiency than the acidic-based $Bi_2Mo_2O_9$. The doping of Eu^{3+} increased the photocatalytic activity of acidic-based $Bi_2Mo_2O_9$, and the efficiency increased as the percentage of Eu^{3+} increased. The 10% doping of Eu^{3+} on $Bi_2Mo_2O_9$ synthesised in an acetic acid medium resulted in the complete degradation of the dye within 4 hours.

DAFT

Acknowledgments

The authors would like to express their gratitude to Deanship of Scientific Research at King Khalid University, Abha, Saudi Arabia for funding this work through Research Groups Program under Grant No. R.G.P.2/249/43.

Declaration of conflict of interest

None to declare

Data availability statement

The raw/processed data required to reproduce these findings cannot be shared at this time as the data also forms part of an ongoing study

Author contributions

Priyadharshini Shanmugam, Thangaraju Dheivasigamani, S. Moorthy Babu, R. Marnadu: *Conceptualization, Data curation, Formal analysis, Writing - original draft,* ***S. AlFaify, Mohd. Shkir, Vasudeva Reddy Minnam Reddy:*** *Funding acquisition, Investigation, Methodology, Project administration, Resources, Software, Supervision, Validation, Visualization, Writing - review and editing.*

REFERENCES

[1] S. Batool, A. Khalid, K.C.A. Jalal, M. Sarfraz, K.S. Balkhair, M.A. Ashraf, Effect of azo dye on ammonium oxidation process and ammonia-oxidizing bacteria (AOB) in soil, RSC Adv. 5 (2015). https://doi.org/10.1039/c5ra03768a.

[2] V. Jassal, U. Shanker, B.S. Kaith, S. Shankar, Green synthesis of potassium zinc hexacyanoferrate nanocubes and their potential application in photocatalytic degradation of organic dyes, RSC Adv. 5 (2015) 26141–26149. https://doi.org/10.1039/c5ra03266k.

[3] M.M.J. Sadiq, U.S. Shenoy, D.K. Bhat, NiWO4-ZnO-NRGO ternary nanocomposite as an efficient photocatalyst for degradation of methylene blue and reduction of 4-nitro phenol, J. Phys. Chem. Solids. 109 (2017) 124–133. https://doi.org/10.1016/j.jpcs.2017.05.023.

[4] S. Sansuk, S. Srijaranai, S. Srijaranai, A New Approach for Removing Anionic Organic Dyes from Wastewater Based on Electrostatically Driven Assembly, Environ. Sci. Technol. 50 (2016) 6477–6484. https://doi.org/10.1021/acs.est.6b00919.

[5] Y. Zheng, L. Cao, G. Xing, Z. Bai, J. Huang, Z. Zhang, Microscale flower-like magnesium oxide for highly efficient photocatalytic degradation of organic dyes in aqueous solution, RSC Adv. 9 (2019) 7338–7348. https://doi.org/10.1039/C8RA10385B.

DRAFT

[6] J. Theerthagiri, R.A. Senthil, A. Malathi, A. Selvi, J. Madhavan, M. Ashokkumar, Synthesis and characterization of a CuS-WO3 composite photocatalyst for enhanced visible light photocatalytic activity, RSC Adv. 5 (2015) 52718–52725. https://doi.org/10.1039/c5ra06512g.

[7] S.A. Khan, S.B. Khan, A.M. Asiri, Toward the design of Zn-Al and Zn-Cr LDH wrapped in activated carbon for the solar assisted de-coloration of organic dyes, RSC Adv. 6 (2016) 83196–83208. https://doi.org/10.1039/c6ra10598j.

[8] Y. Li, H. Wang, S. Peng, Tunable photodeposition of MoS2 onto a composite of reduced graphene oxide and CdS for synergic photocatalytic hydrogen generation, J. Phys. Chem. C. 118 (2014) 19842–19848. https://doi.org/10.1021/jp5054474.

[9] Y. Yu, S. Huang, Y. Lin, J. Yang, X. Li, J. Zhang, J. Yu, H. Shi, W. Wang, Enhanced photocatalytic activity and stability of semiconductor by Ag doping and simultaneous deposition: The case of CdS, RSC Adv. 3 (2013) 20782–20792. https://doi.org/10.1039/c3ra42445f.

[10] L. Huang, X. Wang, J. Yang, G. Liu, J. Han, C. Li, Dual cocatalysts loaded type i CdS/ZnS core/shell nanocrystals as effective and stable photocatalysts for H2 evolution, J. Phys. Chem. C. 117 (2013) 11584–11591. https://doi.org/10.1021/jp400010z.

[11] S. Balachandran, M. Swaminathan, Facile fabrication of heterostructured Bi2O3-ZnO photocatalyst and its enhanced photocatalytic activity, J. Phys. Chem. C. 116 (2012) 26306–26312. https://doi.org/10.1021/jp306874z.

[12] J. Zhang, L. Zhang, N. Yu, K. Xu, S. Li, H. Wang, J. Liu, Flower-like Bi2S3/Bi2MoO6 heterojunction superstructures with enhanced visible-light-driven photocatalytic activity, RSC Adv. 5 (2015) 75081–75088.

DRAFT

https://doi.org/10.1039/c5ra13148k.

[13] Y. Hao, X. Dong, S. Zhai, X. Wang, H. Ma, X. Zhang, Towards understanding the photocatalytic activity enhancement of ordered mesoporous Bi2MoO6 crystals prepared via a novel vacuum-assisted nanocasting method, RSC Adv. 6 (2016) 35709–35718. https://doi.org/10.1039/c6ra05796a.

[14] S.Y. Lu, Y.N. Yu, S.J. Bao, S.H. Liao, In situ synthesis and excellent photocatalytic activity of tiny Bi decorated bismuth tungstate nanorods, RSC Adv. 5 (2015) 85500–85505. https://doi.org/10.1039/c5ra15406e.

[15] Y. Chen, T. Shi, P. Liu, X. Ma, L. Shui, C. Shang, Z. Chen, X. Wang, K. Kempa, G. Zhou, Insights into the mechanism of the enhanced visible-light photocatalytic activity of black phosphorus/BiVO4 heterostructure: A first-principles study, J. Mater. Chem. A. 6 (2018) 19167–19175. https://doi.org/10.1039/c8ta07321j.

[16] N. Wetchakun, S. Chaiwichain, B. Inceesungvorn, K. Pingmuang, S. Phanichphant, A.I. Minett, J. Chen, BiVO 4/CeO 2 nanocomposites with high visible-light-induced photocatalytic activity, ACS Appl. Mater. Interfaces. 4 (2012) 3718–3723. https://doi.org/10.1021/am300812n.

[17] V. Ponec, Catalysis, science and technology, Appl. Catal. 6 (1983) 385. https://doi.org/10.1016/0166-9834(83)80125-0.

[18] G. Yang, Y. Liang, K. Li, J. Yang, R. Xu, X. Xie, Construction of a Ce3+ doped CeO2/Bi2MoO6 heterojunction with a mutual component activation system for highly enhancing the VIsible-light photocatalytic actiVIty for removal of TC or Cr(VI), Inorg. Chem. Front. 6 (2019) 1507–1517. https://doi.org/10.1039/c9qi00302a.

[19] Z. Hao, L. Xu, B. Wei, L. Fan, Y. Liu, M. Zhang, H. Gao, Nanosize α-Bi2O3

DRAFT

decorated Bi2MoO6via an alkali etching process for enhanced photocatalytic performance, RSC Adv. 5 (2015) 12346–12353. https://doi.org/10.1039/c4ra14184a.

[20] E.L. Cuéllar, A. Martínez-De La Cruz, K.H.L. Rodríguez, U.O. Méndez, Preparation of γ-Bi2MoO6 thin films by thermal evaporation deposition and characterization for photocatalytic applications, Catal. Today. 166 (2011) 140–145. https://doi.org/10.1016/j.cattod.2010.05.005.

[21] D. Chen, Q. Hao, Z. Wang, H. Ding, Y. Zhu, Influence of phase structure and morphology on the photocatalytic activity of bismuth molybdates, CrystEngComm. 18 (2016) 1976–1986. https://doi.org/10.1039/c6ce00264a.

[22] P. Sprenger, W. Kleist, J.D. Grunwaldt, Recent Advances in Selective Propylene Oxidation over Bismuth Molybdate Based Catalysts: Synthetic, Spectroscopic, and Theoretical Approaches, ACS Catal. 7 (2017) 5628–5642. https://doi.org/10.1021/acscatal.7b01149.

[23] J.F. Brazdil, Scheelite: A versatile structural template for selective alkene oxidation catalysts, Catal. Sci. Technol. 5 (2015) 3452–3458. https://doi.org/10.1039/c5cy00387c.

[24] D. Zhou, H. Wang, X. Yao, L.X. Pang, Microwave dielectric properties of low temperature firing Bi 2Mo2O9 ceramic, J. Am. Ceram. Soc. 91 (2008) 3419–3422. https://doi.org/10.1111/j.1551-2916.2008.02596.x.

[25] C. Guo, J. Xu, S. Wang, L. Li, Y. Zhang, X. Li, Facile synthesis and photocatalytic application of hierarchical mesoporous Bi 2MoO 6 nanosheet-based microspheres, CrystEngComm. 14 (2012) 3602–3608. https://doi.org/10.1039/c2ce06757a.

[26] S. Baduri, D. Sariket, D. Ray, S. Ghosh, J.K. Singh, H.S. Lee, C. Bhattacharya,

DRAFT

Optimization of semiconductor–electrolyte interfacial phenomena for stable and efficient photoelectrochemical water oxidation behavior of Bi2Mo2O9–Bi2MoO6 heterojunction, Electrochim. Acta. 372 (2021) 137754. https://doi.org/10.1016/j.electacta.2021.137754.

[27] R. Kumar, A. Sudhaik, P. Raizada, A. Hosseini-Bandegharaei, V.K. Thakur, A. Saini, V. Saini, P. Singh, An overview on bismuth molybdate based photocatalytic systems: Controlled morphology and enhancement strategies for photocatalytic water purification, J. Environ. Chem. Eng. 8 (2020) 104291. https://doi.org/10.1016/j.jece.2020.104291.

[28] H. Li, W. Li, X. Liu, C. Ren, F. Wang, X. Miao, Fabrication of bismuth molybdate photocatalyst co-substituted by gadolinium and tungsten for bismuth and molybdenum: Design and radical regulating by the synergistic effect of redox centers and oxygen vacancies for boosting photocatalytic activity, J. Taiwan Inst. Chem. Eng. 89 (2018) 86–94. https://doi.org/10.1016/j.jtice.2018.04.014.

[29] L. Yang, C. Du, S. Tan, Z. Zhang, J. Song, Y. Su, Y. Zhang, S. Wang, G. Yu, H. Chen, L. Zhou, J. Chen, Improved photocatalytic properties of Fe(III) ion doped Bi2MoO6 for the oxidation of organic pollutants, Ceram. Int. 47 (2021) 5786–5794. https://doi.org/10.1016/j.ceramint.2020.10.165.

[30] H. Li, W. Li, X. Liu, C. Ren, X. Miao, X. Li, Engineering of Gd/Er/Lu-triple-doped Bi 2 MoO 6 to synergistically boost the photocatalytic performance in three different aspects: Oxidizability, light absorption and charge separation, Appl. Surf. Sci. 463 (2019) 556–565. https://doi.org/10.1016/j.apsusc.2018.08.254.

[31] A.A. Alemi, R. Kashfi, B. Shabani, Preparation and characterization of novel Ln (Gd3+, Ho 3+ and Yb3+)-doped Bi2MoO6 with Aurivillius layered structures and

DRAFT

photocatalytic activities under visible light irradiation, J. Mol. Catal. A Chem. 392 (2014) 290–298. https://doi.org/10.1016/j.molcata.2014.05.029.

[32] S. Chen, Y. Li, Z. Wu, B. Wu, H. Li, F. Li, Enhanced photocatalytic activity of Te-doped Bi2MoO6 under visible light irradiation: Effective separation of photogenerated carriers resulted from inhomogeneous lattice distortion and improved electron capturing ability, J. Solid State Chem. 249 (2017) 124–130. https://doi.org/10.1016/j.jssc.2017.02.027.

[33] J. Song, L. Zhang, J. Yang, X.H. Huang, J.S. Hu, Facile hydrothermal synthesis of Fe3+ doped Bi2Mo2O9 ultrathin nanosheet with improved photocatalytic performance, Ceram. Int. 43 (2017) 9214–9219. https://doi.org/10.1016/j.ceramint.2017.04.075.

[34] H. Yu, Z. Zhu, J. Zhou, J. Wang, J. Li, Y. Zhang, Self-assembly and enhanced visible-light-driven photocatalytic activities of Bi 2 MoO 6 by tungsten substitution, Appl. Surf. Sci. 265 (2013) 424–430. https://doi.org/10.1016/j.apsusc.2012.11.023.

[35] A. Durairajan, D. Balaji, K. Kavi Rasu, S. Moorthy Babu, M.A. Valente, D. Thangaraju, Y. Hayakawa, Sol-gel synthesis and photoluminescence analysis of Sm3+:NaGd(WO4)2 phosphors, J. Lumin. 170 (2016) 743–748. https://doi.org/10.1016/j.jlumin.2015.08.013.

[36] D. Thangaraju, A. Durairajan, D. Balaji, S. Moorthy Babu, Y. Hayakawa, SiO 2/KGd(WO 4) 2:Eu 3+ composite luminescent nanoparticles: Synthesis and characterization, Mater. Chem. Phys. 135 (2012) 1115–1121. https://doi.org/10.1016/j.matchemphys.2012.06.031.

[37] A. Durairajan, D. Thangaraju, D. Balaji, S. Moorthy Babu, Sol-gel synthesis and characterizations of crystalline NaGd(WO 4)2 powder for anisotropic transparent

DRAFT

ceramic laser application, Opt. Mater. (Amst). 35 (2013) 740–743. https://doi.org/10.1016/j.optmat.2012.08.018.

[38] D. Balaji, A. Durairajan, D.thangaraju, K. Kavi Rasu, S. Moorthy Babu, Investigation of structural and luminescent properties of Pr3+ activated CsGd(WO4)2 by sol-gel synthesis, Mater. Sci. Eng. B Solid-State Mater. Adv. Technol. 178 (2013) 762–767. https://doi.org/10.1016/j.mseb.2013.03.008.

[39] D. Thangaraju, A. Durairajan, D. Balaji, S. Moorthy Babu, Synthesis and characterization of monoclinic KGd(WO4) 2 particles for non-cubic transparent ceramics, Opt. Mater. (Amst). 35 (2013) 753–756. https://doi.org/10.1016/j.optmat.2012.09.018.

[40] S. Selvakumar, R. Manivasagan, K. Chinnappan, Biodegradation and decolourization of textile dye wastewater using Ganoderma lucidum, 3 Biotech. 3 (2013) 71–79. https://doi.org/10.1007/s13205-012-0073-5.

[41] A. Phuruangrat, P. Jitrou, P. Dumrongrojthanath, N. Ekthammathat, B. Kuntalue, S. Thongtem, T. Thongtem, Hydrothermal synthesis and characterization of Bi2MoO 6 nanoplates and their photocatalytic activities, J. Nanomater. 2013 (2013). https://doi.org/10.1155/2013/789705.

[42] K. Seevakan, A. Manikandan, P. Devendran, Y. Slimani, A. Baykal, T. Alagesan, Structural, magnetic and electrochemical characterizations of Bi2Mo2O9 nanoparticle for supercapacitor application, J. Magn. Magn. Mater. 486 (2019) 165254. https://doi.org/10.1016/j.jmmm.2019.165254.

[43] T. Thiyagarajan, V. Deivasigamani, M. Raj, C. Joseph, T. Dheivasigamani, B. Palanivel, M.S. Hamdy, M. Shkir, Facile synthesis and characterization of WO3/CuWO4 nanocomposites for the removal of toxic methylene blue dye, Korean J.

DRAFT

Chem. Eng. 38 (2021) 952–965. https://doi.org/10.1007/s11814-021-0756-x.

[44] Z.R. Khan, M. Shkir, T. Alshahrani, M.A. Manthrammel, S. AlFaify, Facile microwave synthesis of bismuth molybdate nanostructures and their characterization for optoelectronic applications, Solid State Sci. 107 (2020) 106361. https://doi.org/10.1016/j.solidstatesciences.2020.106361.

[45] B. Shunmughananthan, T. Dheivasigamani, J. Sthevan Kovil Pitchai, S. Periyasamy, Performance comparison of distinct bismuth molybdate single phases for asymmetric supercapacitor applications, Dalt. Trans. (2022). https://doi.org/10.1039/d2dt02092k.

[46] R. Gupta, Santosh K and Sahu, M and Ghosh, PS and Tyagi, Deepak and Saxena, MK and Kadam, Energy transfer dynamics and luminescence properties of Eu 3+ in CaMoO 4 and SrMoO 4, Dalt. Trans. 44 (1972) 18957-18969.

[47] H. Wang, X. Liu, P. Niu, S. Wang, J. Shi, L. Li, Porous Two-Dimensional Materials for Photocatalytic and Electrocatalytic Applications, Matter. 2 (2020) 1377–1413. https://doi.org/10.1016/j.matt.2020.04.002.

[48] V. Santhana, D. Thangaraju, A. Tanaka, W. Inami, S. JayaKumar, S. Matsuda, Development of Hybrid TiO2/Paint Sludge Extracted Microbe Composite for Enhanced Photocatalytic Dye Degradation, J. Inorg. Organomet. Polym. Mater. 30 (2020) 2805–2813. https://doi.org/10.1007/s10904-020-01448-2.

[49] J. Liqiang, Q. Yichun, W. Baiqi, L. Shudan, J. Baojiang, Y. Libin, F. Wei, F. Honggang, S. Jiazhong, Review of photoluminescence performance of nano-sized semiconductor materials and its relationships with photocatalytic activity, Sol. Energy Mater. Sol. Cells. 90 (2006) 1773–1787. https://doi.org/10.1016/j.solmat.2005.11.007.

[50] K. Qi, B. Cheng, J. Yu, W. Ho, Review on the improvement of the photocatalytic and

DRAFT

antibacterial activities of ZnO, J. Alloys Compd. 727 (2017) 792–820. https://doi.org/10.1016/j.jallcom.2017.08.142.

[51] H.H. Li, K.W. Li, H. Wang, Hydrothermal synthesis and photocatalytic properties of bismuth molybdate materials, Mater. Chem. Phys. 116 (2009) 134–142. https://doi.org/10.1016/j.matchemphys.2009.02.058.

[52] P. Dumrongrojthanath, T. Thongtem, A. Phuruangrat, S. Thongtem, Synthesis of Bi2MoO6 nanoplates with the assistance of PEG by hydrothermal method and their photocatalytic activities, Dig. J. Nanomater. Biostructures. 9 (2014) 593–598.

[53] A.R. J. Rodríguez-Lópeza, R. Rangela, P. Bartolo-Pérezb, J.J. Alvarado-Gilb, J. L. Cervantes-Lópezb, R. Garcíac, Photocatalytic Degradation of 2-chlorophenol under γ-Bi2MoO6/Graphene Oxide, MRS Adv. 5 (2020) 581–589. https://doi.org/10.1557/adv.2019.414.

[54] M. Waqar, M. Imran, S.F. Adil, S. Noreen, S. Latif, M. Khan, M.R.H. Siddiqui, Enhanced photoluminescence and photocatalytic efficiency of la-doped bismuth molybdate: Its preparation and characterization, Materials (Basel). 13 (2020). https://doi.org/10.3390/ma13010035.

[55] P. Dumrongrojthanath, T. Thongtem, A. Phuruangrat, S. Thongtem, Glycothermal synthesis of Dy-doped Bi2MoO6 nanoplates and their photocatalytic performance, Res. Chem. Intermed. 42 (2016) 5087–5097. https://doi.org/10.1007/s11164-015-2346-1.

[56] M. Kristl, N. Sinanović, S. Gyergyek, J. Kristl, Sonochemical synthesis, characterization and photocatalytic activity of Bi2Mo3O12, Inorg. Chem. Commun. 112 (2020) 107699. https://doi.org/10.1016/j.inoche.2019.107699.

DRAFT

[57] P. Suresh, A. Umabala, A. Rao, Rapid sun light degradation of Rhodamine-B, Methylene blue, Methyl orange, Congo red and their binary mixtures using suprastoichiometric Bi - Molybdate, Int. J. Eng. Appl. Sci. 2 (2015) 257851.

[58] F. Wang, X. Zhou, J. Li, Q. He, L. Zheng, Q. Liu, Y. Chen, G. Zhang, X. Liu, H. Li, Rationally designed bi2m2o9 (M = mo/w) photocatalysts with significantly enhanced photocatalytic activity, Molecules. 26 (2021) 1–15. https://doi.org/10.3390/molecules26237334.

DRAFT

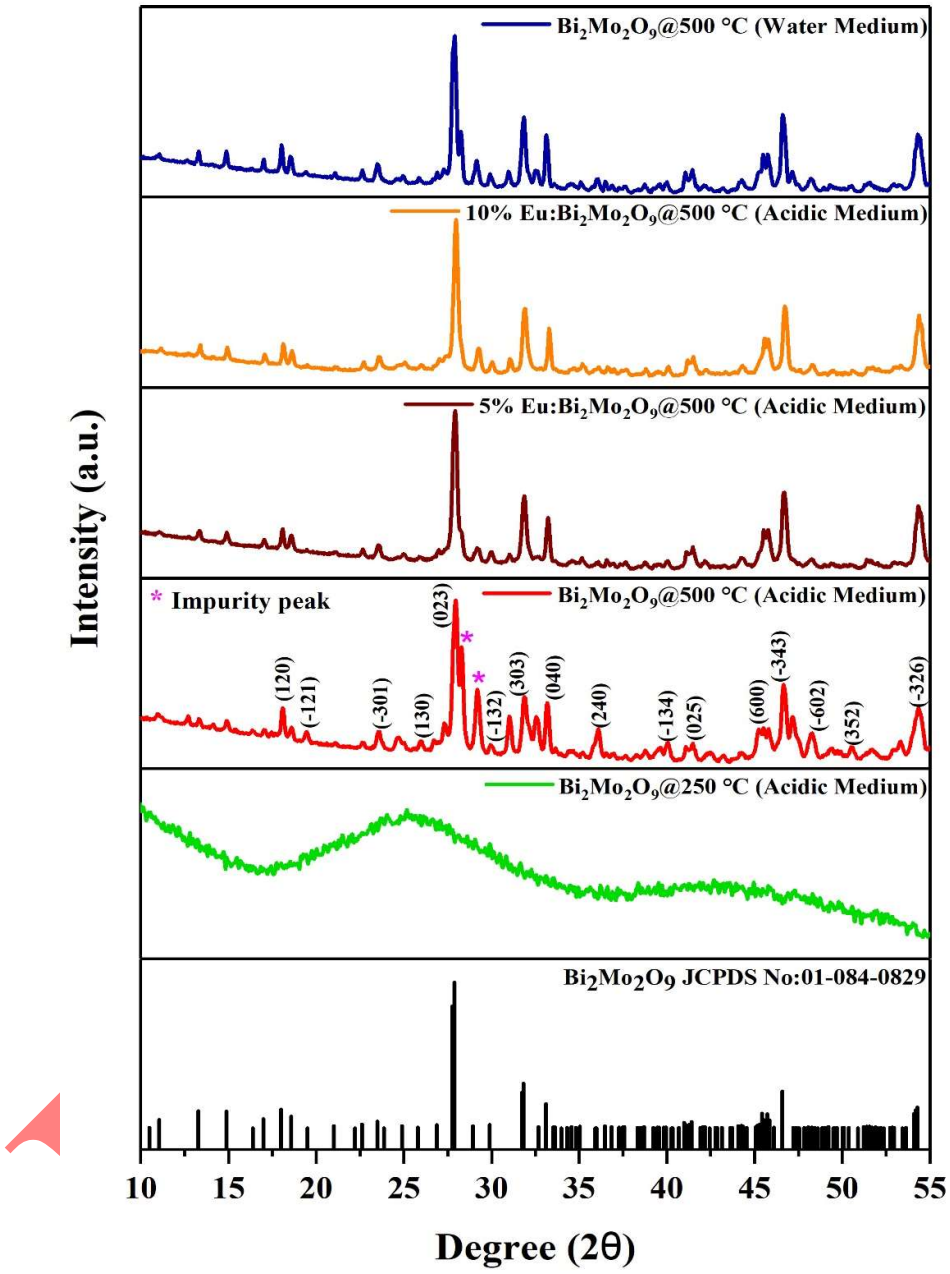

Figure 1: Comparitive XRD pattern of $Bi_2Mo_2O_9$ @250°C (acidic medium), $Bi_2Mo_2O_9$ @500°C (acidic medium), 5%Eu: $Bi_2Mo_2O_9$ @500°C (acidic medium), 10%Eu: $Bi_2Mo_2O_9$ @500°C (acidic medium), $Bi_2Mo_2O_9$ @500°C (water medium).

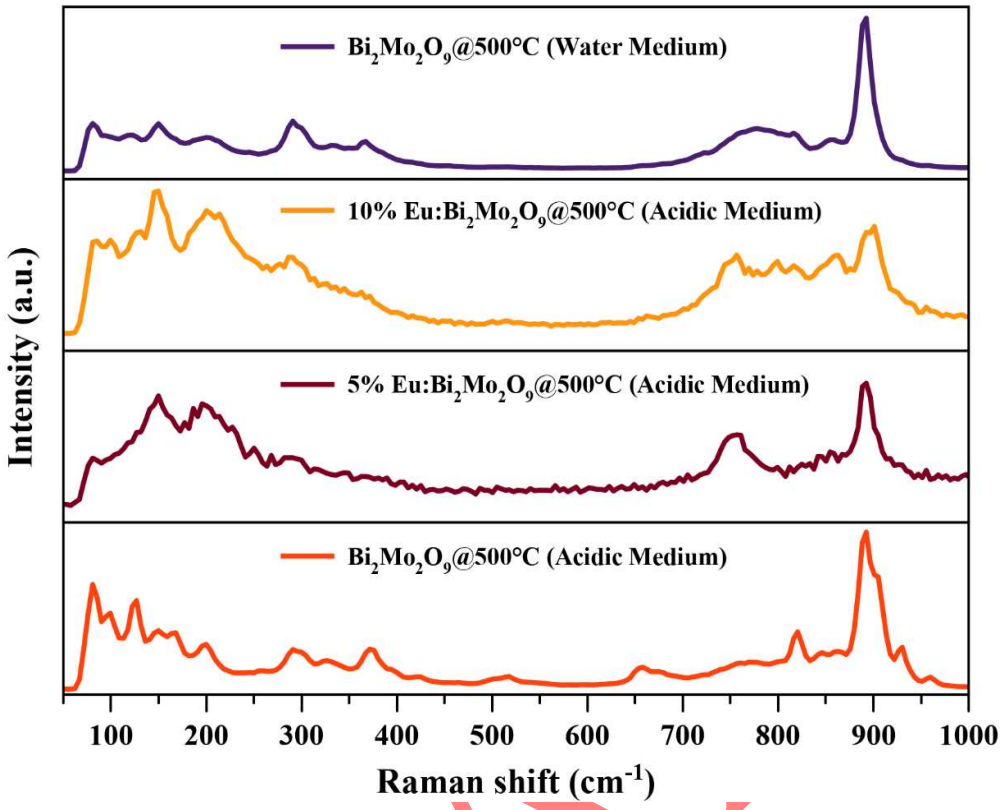

Figure 2: Comparative Raman spectra of $Bi_2Mo_2O_9$ @500°C (acidic medium), 5%Eu: $Bi_2Mo_2O_9$ @500°C (acidic medium), 10%Eu: $Bi_2Mo_2O_9$ @500°C (acidic medium), $Bi_2Mo_2O_9$ @500°C (water medium).

DRAFT

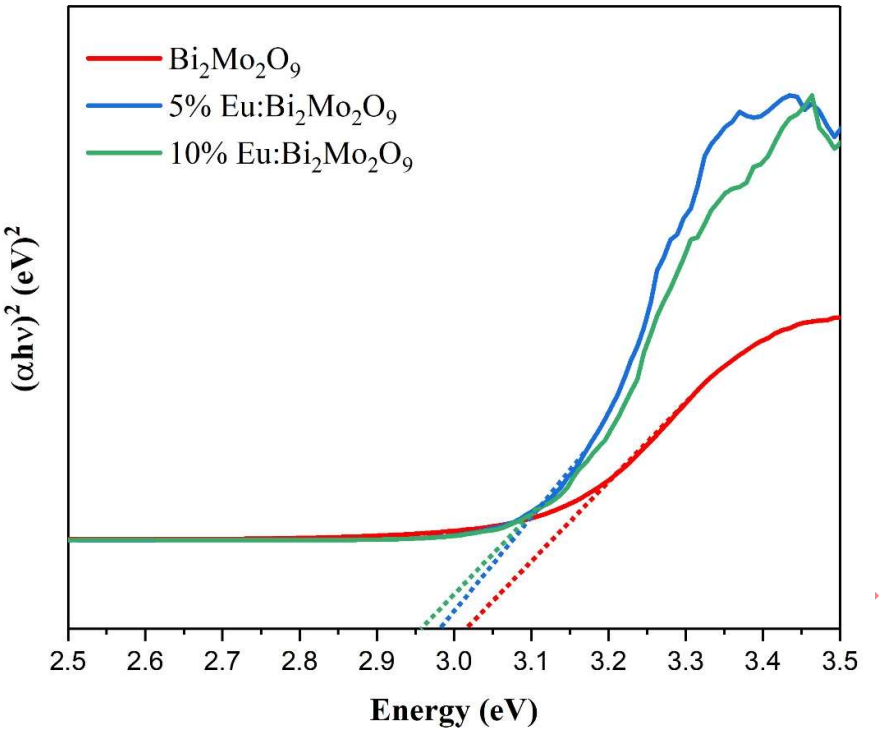

Figure 3: Tau plot of $Bi_2Mo_2O_9$, 5%Eu: $Bi_2Mo_2O_9$ and 10%Eu: $Bi_2Mo_2O_9$

DRAFT

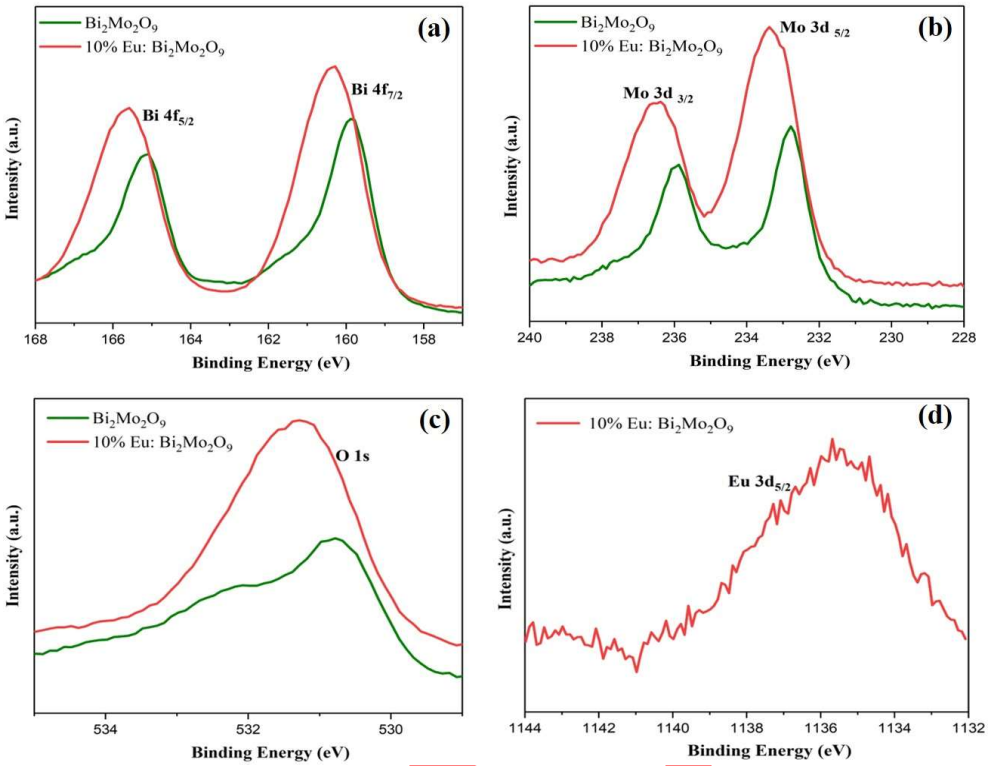

Figure 4: XPS graphs of Bi 4f (a), Mo 3d (b), O 1s (c) and Eu 3d (d) for $Bi_2Mo_2O_9$ and 10%Eu: $Bi_2Mo_2O_9$

DRAFT

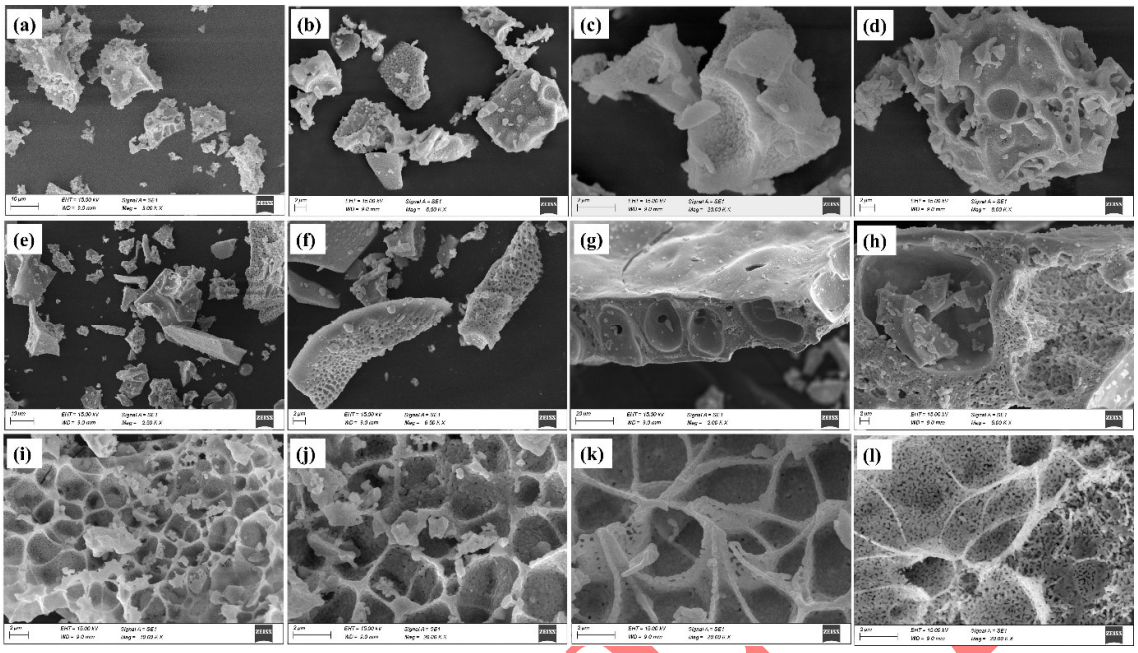

Figure 5: SEM images of $Bi_2Mo_2O_9$ @500°C in acidic medium (a-d), 5%Eu: $Bi_2Mo_2O_9$ @500°C in acidic medium (e-h), 10%Eu: $Bi_2Mo_2O_9$ @500°C in acidic medium (i-l).

DRAFT

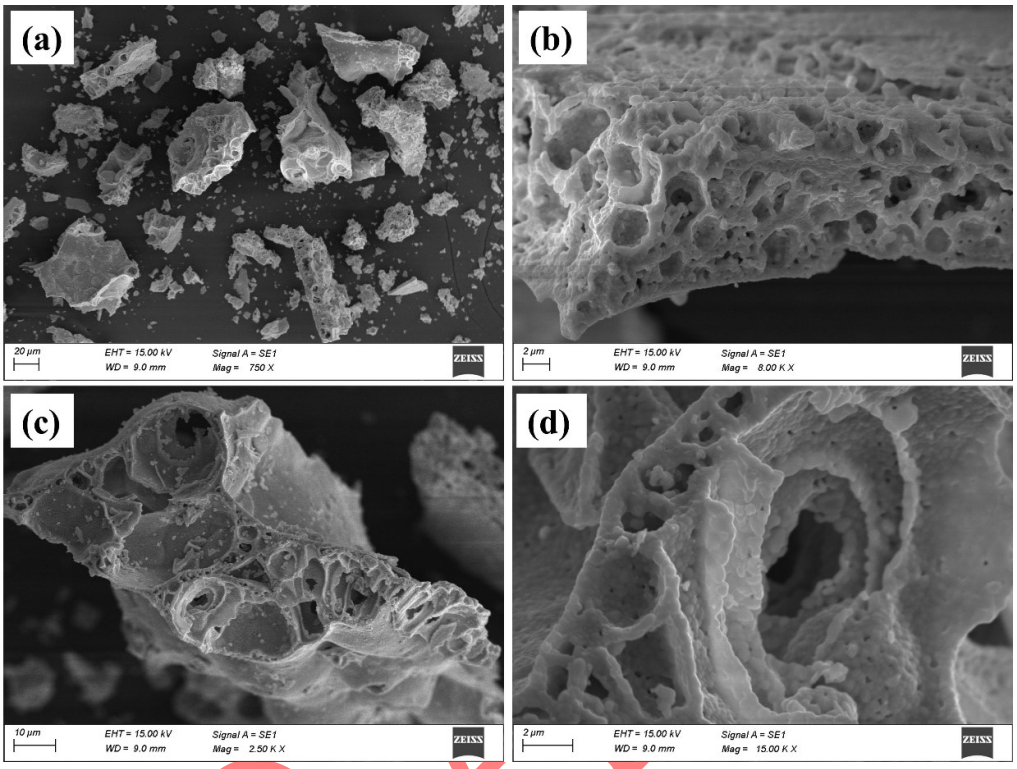

Figure 6: SEM images of $Bi_2Mo_2O_9$ @500°C in acidic medium (a&b), $Bi_2Mo_2O_9$ @500°C in water medium (c&d).

DRAFT

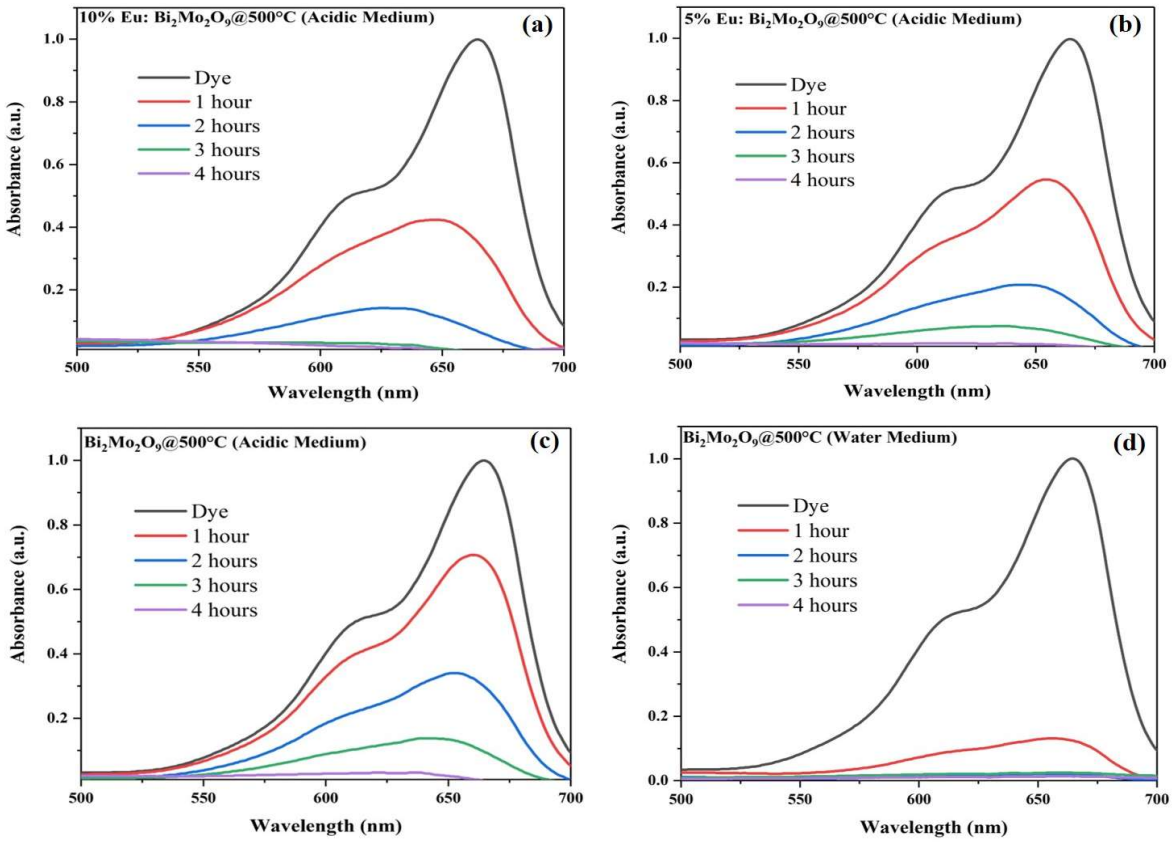

Figure 7: Photocatalytic degradation of methylene blue using $Bi_2Mo_2O_9$ @500°C in acidic medium (a), 5%Eu: $Bi_2Mo_2O_9$ @500°C in acidic medium (b), 10%Eu: $Bi_2Mo_2O_9$ @500°C in acidic medium (c), $Bi_2Mo_2O_9$ @500°C in water medium (d).

DK

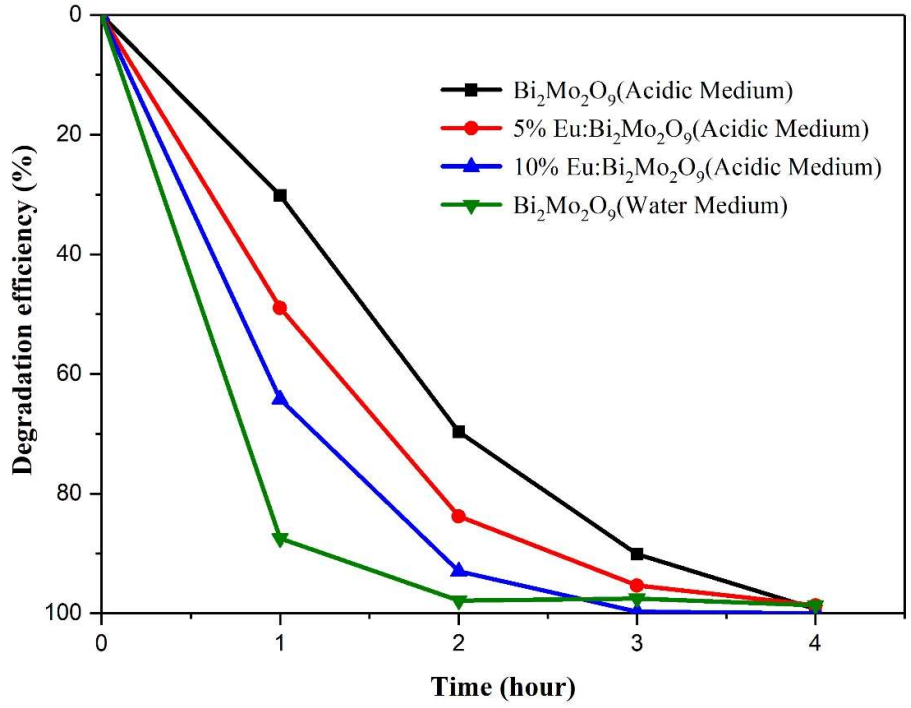

Figure 8: Degradation percentage of Methylene blue on $Bi_2Mo_2O_9$ @500°C in acidic medium, 5%Eu: $Bi_2Mo_2O_9$ @500°C in acidic medium, 10%Eu: $Bi_2Mo_2O_9$ @500°C in acidic medium, $Bi_2Mo_2O_9$ @500°C in water medium.

DRAFT

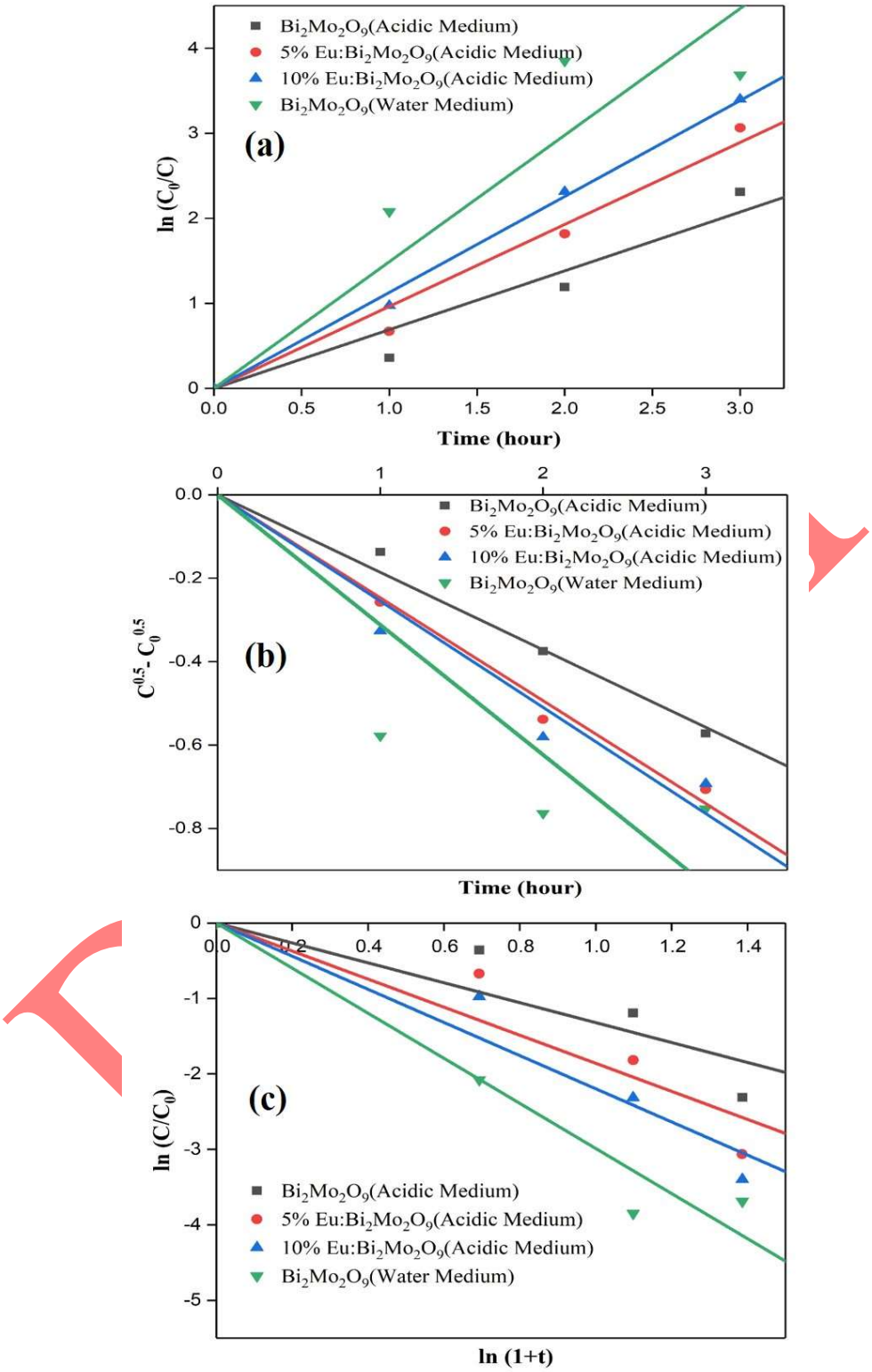

Figure 9: The kinetic plot for the degradation of methylene blue

Table 1: Comparison of photocatalytic activity of β-$Bi_2Mo_2O_9$ with other phases of bismuth molybdate.

Photocatalyst	Synthesis route	Targeted pollutant	Result	Ref
α-$Bi_2Mo_3O_{12}$ β-$Bi_2Mo_2O_9$ γ-Bi_2MoO_6	Hydrothermal method	Rhodamine B	The γ-Bi_2MoO_6 shows excellent photocatalytic activity among the three phases with efficiency of 65.7% in 150 min.	[51]
Bi_2MoO_6 nanoplates	PEG assist Hydrothermal method	Rhodamine B	The photocatalytic activity was about 95.02% within 100 min of time.	[52]
N doped Bi_2MoO_6/GO	Hydrothermal method	2-Chlorophenol	About 80% of the 2-chlorophenol is degraded by N-doped Bi2MoO6/GO within 65 min	[53]
La doped Bi_2MoO_6	Sol-gel method	Methylene blue	The Degradation of MB with Bi_2MoO_6 and La doped Bi_2MoO_6 were found to be 68% and 75% respectively.	[54]
Dy-doped Bi_2MoO_6	Glycothermal method	Rhodamine B	About 97.22% of the RhB is degraded within 80 min	[55]
$Bi_2Mo_3O_{12}$	Sonochemical method	Rhodamine B	Achieved complete degradation after 120 min due to small crystallite size and unique morphology.	[56]
$Bi_2Mo_3O_{12}$	Combustion method	Rhodamine B, Methylene blue, Methyl orange, Cango red	Complete degradation of RhB, MB, MO and cango red within 60 min, 120 min, 70min and 60 min respectively.	[57]
Fe3+ doped $Bi_2Mo_2O_9$	Hydrothermal method	Rhodamine B	1.5% Fe3+ doped $Bi_2Mo_2O_9$ exhibits higher photocatalytic activity which is 6.7 times higher than pure $Bi_2Mo_2O_9$.	[33]
$Bi_2Mo_2O_9$ $Bi_2W_2O_9$	Hydrothermal method	Methylene blue	About 75% of MB is degraded by $Bi_2Mo_2O_9$ within 4 hours.	[58]
Eu doped β-$Bi_2Mo_2O_9$	Sol-gel method	Methylene blue	The water-based β-$Bi_2Mo_2O_9$ shows more dye degradation than acetic-based β-$Bi_2Mo_2O_9$. The 10% Eu: $Bi_2Mo_2O_9$ completely degraded (100%) the MB dye within 4 hours.	This work

DRAFT

Table 2: Kinetic parameters for photocatalytic degradation of methylene blue on $Bi_2Mo_2O_9$ (acidic medium), 5%Eu: $Bi_2Mo_2O_9$ (acidic medium), 10%Eu: $Bi_2Mo_2O_9$ (acidic medium), $Bi_2Mo_2O_9$ (water medium)

Kinetic model	Parameter	$Bi_2Mo_2O_9$ (Acidic Medium)	5%Eu:$Bi_2Mo_2O_9$ (Acidic Medium)	10%Eu:$Bi_2Mo_2O_9$ (Acidic Medium)	$Bi_2Mo_2O_9$ (Water Medium)
First order model	Rate constant	0.6914	0.9641	1.1283	1.4886
	R^2 (COD)	0.9706	0.9903	0.9984	0.9886
Diffusion model	Rate constant	-0.185	-0.246	-0.254	-0.311
	R^2 (COD)	0.9946	0.996	0.983	0.9165
Singh model	Rate constant	-1.3200	-1.85906	-2.196	-2.987
	R^2 (COD)	0.91204	0.9493	0.97562	0.94385

DRAFT